

First Year Report - Nanowire Project

Adam West

Durham University - Department of Physics, Durham University, South Road, Durham, DH1 3LE

(Dated: August 28, 2009)

This report documents the progress that has taken place within the ‘nanowire project’. Details of the work on the experimental setup are described, as well as the theoretical considerations which have been investigated. In particular, the optical and vacuum chamber setup is detailed, and explanations of simulations of the proposed magnetic atom mirror experiment are presented, along with theoretical and numerical analysis of the feasibility and quantitative characterisation of the production of tightly confining mobile atom traps, based on single domain wall magnetic potentials. An introduction to nanowires is also provided, and a brief explanation of why they are the source of interesting research.

Contents

1. Introduction	1
1.1. Motivation	1
1.2. Nanowires	1
2. Experimental Setup Progress	2
3. A Magnetic Atom Mirror	4
3.1. Theory	4
3.2. Previous Work	4
3.3. Nanowire Mirror	5
4. Mobile Atom Trap	9
4.1. TOP Traps	10
4.2. RF Dressing	11
5. Outlook	13
A. Polarisation Spectroscopy	13
B. Ioffe-Pritchard Trap	15
References	16

1. INTRODUCTION

1.1. Motivation

The field of research in cold atoms has become a burgeoning and diverse one since its development in the 1980s [1, 2]. A plethora of techniques exist to manipulate cold atoms, using light and electric and magnetic fields. This project combines such cold atoms with nanomagnetic structures - another field which has developed a great deal in its own right. However, research which combines these two fields has been limited. Numerous experiments and theoretical investigations into the interaction of cold atoms with micromagnetic and microelectric structures have been carried out [3–7] and purely optical manipulation of atoms continues with a variety of applications [8–10], yet physics which combines both nanoscale magnetic structures and ultracold atoms has not been as heavily investigated as either aspect in isolation.

The interesting feature of this project is the fact that the length scale of interest is significantly less, simply due to the size of the nanowires. Also, the use of these nanomagnetic structures affords a great deal of freedom, as fabrication techniques are sufficiently advanced so as to allow structures to be made in all kinds of shapes, and it is the choice of shape that gives rise to the interesting physics, as shall be explained.

The length scale of the wires and the control over their geometry lend themselves to the creation of periodic lattices of magnetic material, which form the basis of magnetic mirrors. Because the size of the wires is so small, the magnetic field gradient produced is much higher than in other atomic or molecular mirrors (e.g. [11, 12]), meaning the closest approach of bouncing atoms is much smaller for a given incoming velocity (approaches of the order of 100 nm are predicted), and the characteristic range over which interaction takes place is also smaller. The former point may allow the opportunity to examine short range surface interaction (see [13]), and the latter makes the idea of a ‘point interaction’ (as with a conventional mirror, or an object bouncing) more valid for the mirror that is created.

The small length scale is also advantageous when considering the creation of atom traps; the fact that nanowires create a high magnetic field gradient means that very tight traps can be formed. It is predicted that mean trap frequencies of the order of $\bar{\nu} = 1$ MHz can be achieved, which is significantly higher than can be achieved in other atom systems [14]. It is hoped that the nanowires will form the basis for traps that are both tightly confining (much more so than other magnetic/electric traps) and have the possibility of being mobile; the traps are based on the magnetisation of the nanowire material, which can be dynamically varied to move the traps. If successful, this will give a medium through which atoms can be precisely and accurately held and transported.

1.2. Nanowires

The nanowires which are being used are made out of Permalloy, which is an Iron-Nickel alloy, with the formula $\text{Ni}_{81}\text{Fe}_{19}$. Crucially, it is a magnetic material, which allows for the formation of domain walls at points

where the direction of magnetisation within the material changes. Permalloy is the chosen material for the nanowires due to a number of beneficial physical properties, such as its negligible magnetocrystalline anisotropy and magnetostriction - characteristics which aren't inherent in Nickel or Iron themselves. The former limits the extent to which the microscopic structure dictates the domain structure, and the latter limits any heating which may be caused by the application of magnetic fields, which may lead to disruption of domain wall structure and noise.

The process by which the nanowires are created is focussed ion beam milling. A thin film of Permalloy is deposited onto the surface of the substrate via thermal evaporation, and then the unwanted material is removed using a focussed beam of Gallium ions, with a typical energy of around 20-30 keV. The size of the focus is around 40 nm. It is possible to use this technique to create intricate nanoscale structures. It is an entirely automated process, but can take a number of days to create nanowire arrays of a macroscopic size (~ 1 mm).

With the freedom afforded by the manufacturing process, a particular shape is chosen for the wires such that magnetic domain walls are formed at specific points. Because of the low magnetocrystalline anisotropy, the domain formation is wholly dictated by the macroscopic shape anisotropy. The shape used is informally referred to as a 'wiggly wire', essentially resembling a sinusoidal wave. The typical size of the nanowires is around 200 nm wide, 30 nm thick (deep) with a 'wavelength' of around a micron, which is similar to parameters in previous studies, e.g. [15, 16]. It is the width and depth of the wire that is of interest, as this defines the size of the domain wall. It is in this sense that the wires are nanoscale. The choice of shape will be discussed further in Section 3.

Once the nanowires are fabricated, they need to be characterised. There are a number of techniques available to do this. For straightforward imaging of the wires, scanning electron microscopy (SEM) [17, 18] is used. An example image of some similar (larger scale) wires is given in Figure 1, below.

Atomic force microscopy (AFM) [19] and magneto-optical kerr effect (MOKE) [20] imaging is also used, although the latter has a substantially lower resolution than SEM and AFM (around $5 \mu\text{m}$). It is desirable to be able to image the magnetic domain structure within the nanowires. For this, magnetic force microscopy (MFM) [21, 22] and scanning hall probe microscopy (SHPM) [23, 24] is used, with the former having higher resolution. This allows for direct analysis of the magnetisation within the nanowire structures. This is an important aspect of the project as the behaviour of the domain walls formed, in particular their response to external magnetic fields, will dictate to some degree the experimental procedure, and how effective the mirrors or traps created are. It is also crucial to do any such characterisation before the chips are incorporated in the experiment; they will be in an ultra high vacuum environment ($< 10^{-7}$ Torr) and the aim is to minimise how often the chamber will need to be opened in order to prolong the lifetime and efficacy of the vacuum components. In this way, good commu-

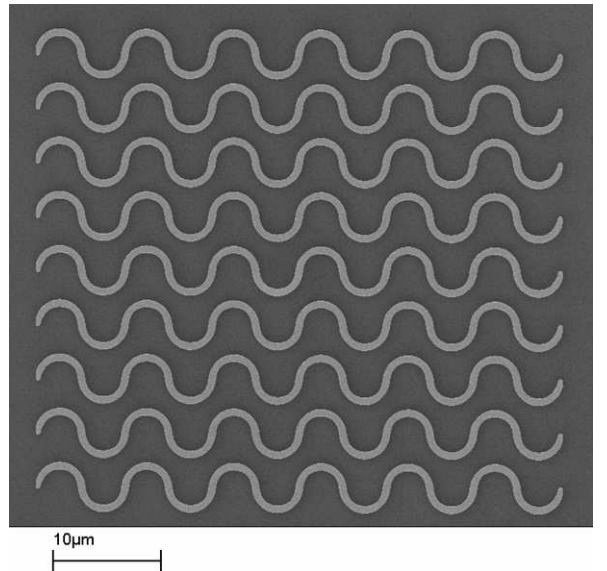


FIG. 1: A scanning electron microscope image of an array of nanowires. The resolution of the image is of the order of nanometres.

nication between the Durham group and colleagues in Sheffield is key to ensuring smooth progress.

It is the domain walls formed in the magnetic nanowires that hold the key to the interesting physics which can be investigated. There are two main experiments which are planned for the nanowire experiment, which consider two different regimes. The 'bulk' field created by many domain walls, relatively far from the material surface, will be used to realise a magnetic atom mirror. Also, the field produced by a single domain wall will be utilised to form a mobile atom trap. These two experiments will be discussed in turn in this report.

2. EXPERIMENTAL SETUP PROGRESS

As the project began in October there has been a great deal of work to be done on the experimental setup, in particular the optics associated with the laser cooling. Rubidium 87 is the species that will be interacting with the nanowire structures. It was chosen as it is commonly used to form a magneto-optical trap and the process is well understood. The energy levels associated with the cooling and repump transitions are shown in Figure 2. As is well known, Rubidium is an excellent candidate for laser cooling due to its accessible closed electronic transition, which is 'pumped'. This is highlighted by the red arrow. Electrons excited to the $5^2P_{3/2}$, $F = 3$ state spontaneously decay after on average 26 ns. However, the field from the laser does not always drive to the $F = 3$ state. The probability of absorption for a given transition has a Lorentzian profile due to homogenous broadening which is described by $g(\omega)$ [26]:

$$g(\omega) = \frac{1}{2\pi} \frac{\Gamma}{(\omega - \omega_0)^2 + \Gamma^2/4}, \quad (1)$$

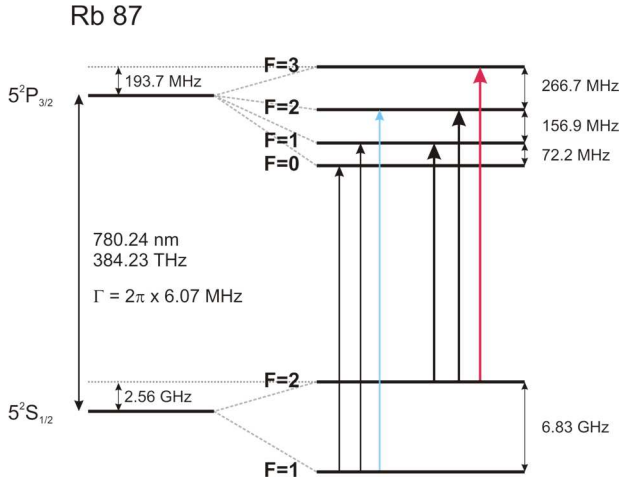


FIG. 2: Energy level diagram for Rubidium 87. The red line shows the pumping transition, and the blue line the repump. Numerical values taken from [25].

where ω is the laser frequency, ω_0 is the frequency of the transition, and Γ is the natural linewidth. Assuming a detuning of twice the natural linewidth, around 0.1% of stimulated transitions will result in the excitation of an electron to the $F = 2$ state. From this state, the electron can spontaneously decay to either the $F = 1$ or $F = 2$ hyperfine ground states instead. The $F = 1$ ground state is ‘dark’ to the pumping field, i.e. the laser frequency is far off resonance from the transition frequency up to a $5^2P_{3/2}$ state. Because of this, a repump laser is also needed, which is highlighted in Figure 2 by the blue arrow. This then excites electrons in this ‘dark’ state back to the upper $F = 2$ state, from where it decays back down to either an $F = 1$ or $F = 2$ state (selection rules prohibit excitation to the $F = 3$ state [27]). The same logic can be applied for the repump transition, but there are only 2 ground state levels so such considerations only add slightly to the population expected in the lower ground state.

The experimental setup uses two separate lasers to generate the pump and repump frequencies. A Toptica DL100 is used to generate pump light, giving out around 100 mW of power, and a home built external cavity diode laser is used to produce the repump light, outputting around 30 mW. The optical setup is shown in Figure 3:

The light is passed through a set of commercial shutters and then coupled into fibers from where it can be directed into chambers as necessary. The shutters have a delay time of around 5 ms (standard deviation around 100 μ s) and a rise time of around 100 μ s (standard deviation around 500 ns). These values are more than satisfactory for our purposes, in particular the variation in these times seems very good. The shutters themselves are isolated from the optical table in order to minimise the effect of any vibrations etc. Computer control of elements within the experimental setup is still under construction and is not required at this stage.

Initial efforts to achieve a MOT were carried out in a simple 6 way cross configuration chamber. Unfortunately these were not successful, and the cause of this was not

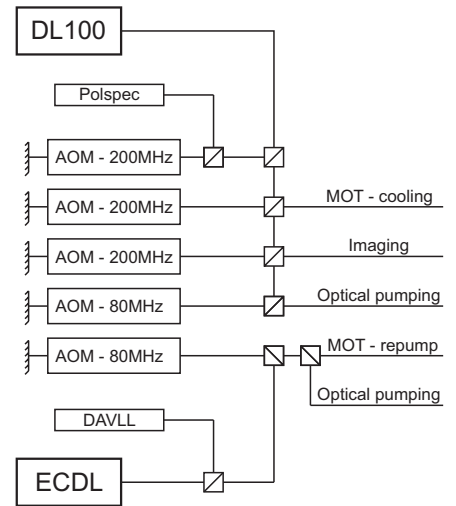


FIG. 3: Diagram of the optical setup used to create the light frequencies necessary for the experiment. Waveplates etc. have been omitted for the sake of clarity.

identified – it was decided that it would be more prudent to move on and use a pyramid MOT as a diagnosis tool – further problems would point to an issue with the optical setup. When the pyramid chamber was used, a MOT was soon created (Figure 4), indicating that the previous troubles were probably not related to the light going into the chamber.

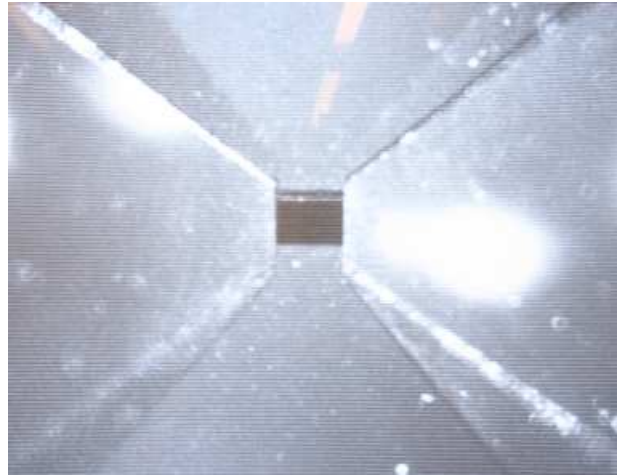


FIG. 4: Cloud of ultracold atoms in the pyramid MOT as imaged with an infrared camera.

The pyramid MOT has now been removed from the setup and the new chamber moved in. Efforts are ongoing to realise a MOT in this new chamber. One diagnostic task for the MOT that has been considered is obtaining an estimate of how many atoms there are. This is done using a sensitive photodiode circuit. The way the atom number is calculated is as follows.

The power of light incident on a photodiode, P_i , is given by

$$P_i = R_\gamma E_\gamma N f, \quad (2)$$

where R_γ is the photon scattering rate from a 2 level atom, E_γ is the photon energy, N is the number of atoms and f is the fractional solid angle over which the light is collected. The current created by the photodiode is then found using its efficiency η in W/A. If the photodiode circuit impedance, Z is known then the output voltage signal, S , can easily be found:

$$\begin{aligned} S &= P_i Z \eta = R_\gamma E_\gamma N f Z \eta \\ &= \frac{\Gamma}{2} \frac{I/I_{\text{sat}}}{4\Delta^2/\Gamma^2 + I/I_{\text{sat}} + 1} \frac{hc}{\lambda} \frac{A}{4\pi R^2} N Z \eta, \end{aligned} \quad (3)$$

where Γ is the natural linewidth, I_{sat} is the saturation intensity, Δ is the detuning, λ the wavelength, A the detector area, R the collector distance and I is the beam intensity, given by $2P/\pi r_{e2}^2$ with P the laser beam power and r_{e2} the $1/e^2$ radius.

For the case of a conventional 3 beam (retroreflected) MOT the beam power after it is split into 3 should be used, and then an additional multiplicative factor of 6 included. For the case of a pyramid MOT the value obtained is an estimate since the intensity of light incident on the atom cloud will depend on its position. This is illustrated in Figure 5. The higher the intensity of the beam across the region of interest the better the estimate is, due to the fact that the scattering force saturates at large intensities.

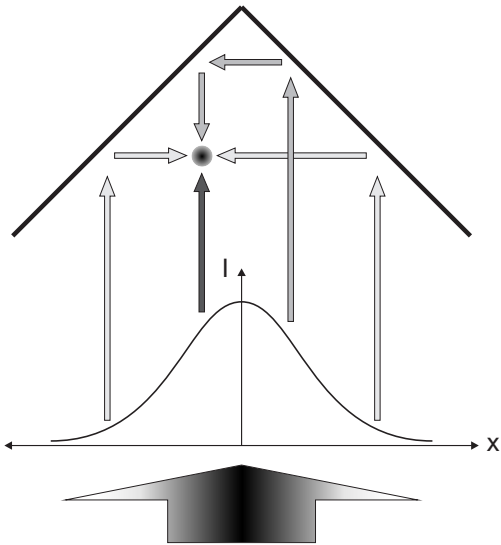


FIG. 5: The beam into a pyramid MOT has a Gaussian intensity profile. Thus the different reflections have different intensities, dependent on the position of the atomic cloud.

In practice it is more sensible to calibrate the photodiode being used than to work with the circuit's effective impedance, as this is often not known accurately. Doing so combines I and η to give an efficiency expressed in volts per watt. The circuit used to collect MOT light replicates that given in [28] and is shown in Figure 6. It allows for variation in gain over 4 orders of magnitude to account for possible variation in parameters, e.g. the number of atoms present or the solid angle collected over.

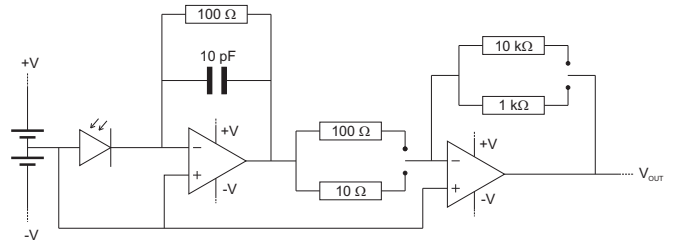


FIG. 6: The photodiode circuit used to collect light from the MOT.

3. A MAGNETIC ATOM MIRROR

3.1. Theory

The reflection of atoms from a surface requires a force to repel them. This is provided by either an electric field or a magnetic field (or combination of the two). In the case of using nanowires to achieve the reflection, it is the magnetic force which is employed.

Atoms interact with magnetic fields because of their magnetic dipole moment. The potential energy for this interaction is given by:

$$\mathcal{H} = -\vec{\mu} \cdot \vec{B} = m_F g_F \mu_B B, \quad (4)$$

where it is assumed that the magnetic dipole is aligned with the external magnetic field. For the case of an inhomogeneous field there is a resulting force which acts on the atom, and is given by:

$$\vec{F} = \vec{\nabla} (\vec{\mu} \cdot \vec{B}) = -m_F g_F \mu_B \vec{\nabla} B. \quad (5)$$

Thus, depending on the values of m_F and g_F , atoms will experience a force towards an area of low or high magnetic field; atoms where $m_F g_F$ is positive are in low field seeking states, and where it is negative, they are in high field seeking states. For atom trapping, low field seeking states are normally used. This formulation is an approximation that is only valid in the weak field regime, as in high fields the magnetic dipole can depend on the applied field.

A magnetic mirror thus relies on the magnetic field gradient it produces. The larger the gradient present, the greater the force, and the more effective a mirror it is.

3.2. Previous Work

The concept of an atom mirror is by no means a new one, and has been previously implemented by a number of people for different species and using a variety of methods [29–31]. The theory behind many of these implementations is very similar though; the mirror surface used has a periodically varying magnetisation within the bulk of the material, as shown in Figure 7(a). This periodic mag-

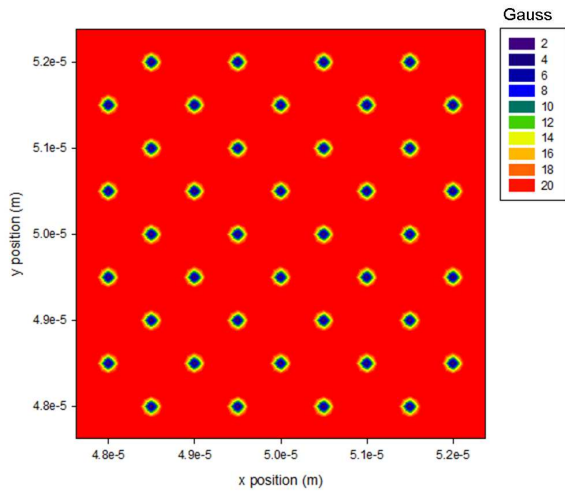


FIG. 9: A contour plot of the calculated magnetic field magnitude at a height of 500 nm due to a 2D array of domain walls produced in nanowires. The wires have a periodicity of $0.5 \mu\text{m}$, a width of 125 nm and a thickness of 30 nm . Figure courtesy of T. Hayward.

1 cm , $m_F = 2$, $g_F = 1/2$ and μ_B is the Bohr magneton. It is assumed that the magnetic dipole of the atom remains aligned with the magnetic field. Thus it is necessary to create a field of at least this strength in order for the atoms to be reflected. The degree of magnetisation within the nanowires will dictate the nature of the field gradient and how far from the surface any atoms will bounce. If the atoms get sufficiently close to the surface, the van der Waals potential will begin to play a role.

For atoms in an $F = 2$ state, the presence of a magnetic field leads to a Zeeman effect which splits the energy state into 5 discrete levels. For the case of an atom, where the nuclear and electron spins are coupled, this leads to the Breit-Rabi effect, and the energy levels do not follow the linear relation one would expect from a simple Zeeman shift. This is illustrated in Figure 10 for the $^{87}\text{Rb } 5^2S_{1/2}$ state in a numerically calculated Breit-Rabi diagram [33].

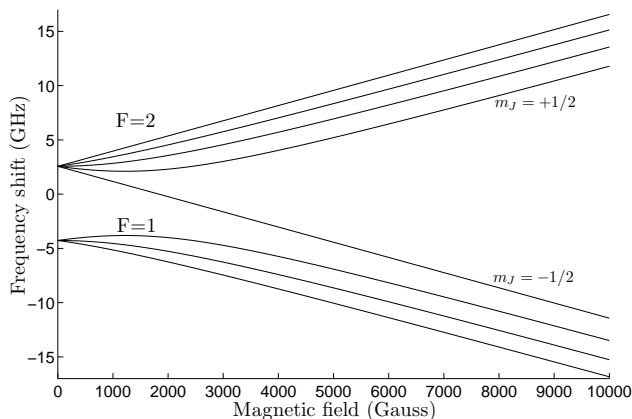


FIG. 10: Breit-Rabi diagram for the $^{87}\text{Rb } 5^2S_{1/2}$ state, showing the non-linear dependence on the magnetic field strength.

The field emanating from the nanowire surface is a

rapidly decaying one, which can be modelled with a $1/r^2$ relationship (a ‘monopole’ model, cf. Section 4.2), and the magnitude of the field is sufficiently large very close to the surface to produce the ‘bending’ of the energy levels observed in the Breit-Rabi diagram. It is expected that the character of the energy levels will be qualitatively similar to that in previous work [13], and Figure 11 shows quantitative predictions of the energy shifts relative to the $5^2S_{1/2}$ ground state for the $F=2$ manifold due to the domain wall field.

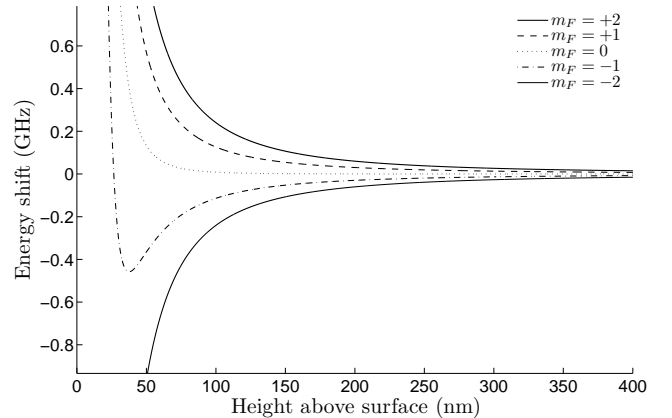


FIG. 11: Energy levels for a Rubidium 85 atom in an $F = 2$ quantum state which have been split due to hyperfine interaction and the Zeeman effect. The energy associated with a Rubidium 87 atom dropped from a height of 1 cm is 21.5 MHz . For the $m_F = +2$ state this is matched by the energy of interaction with the magnetic field at a height of around 330 nm . Calculations assume a wire of width 200 nm and thickness 5 nm .

Sufficiently close to the surface, the interaction due to van der Waals forces begins to dominate, and the potential that atoms experience is modified accordingly. This surface interaction can be well modelled with a Van der Waals potential of the form r^{-3} [34], which derives from a modification of a characteristic r^{-6} dipole-dipole interaction [35] due to its resonant nature. An atom approaching a metal surface will see its ‘mirror image’ as a corresponding dipole is induced in the surface which acts as a zero potential plane. This induced dipole interacts with the atom and produces an energy shift. The process is assumed to be an instantaneous one - a more complete picture is provided by considering Casimir-Polder interactions [36] which are essentially a relativistic phenomenon. It is a good approximation to ignore these interactions considering the small distances and low velocities involved; the modifications made are very small [37], especially considering other uncertainties present. The dipole that is induced is considered to be that with the largest dipole matrix element, which for Rubidium is that associated with the D2 line. The Van der Waals potential, V_v can then be expressed as [38]:

$$V_v(z) = -\frac{\epsilon - 1}{\epsilon + 1} \frac{C^{(3)}}{z^3}, \quad (8)$$

where ε is the dielectric constant of the metal surface, z is the height above this surface and $C^{(3)}$ is the van der Waals coefficient, which is defined as [39, 40]:

$$C^{(3)} = \frac{1}{4\pi} \int_0^\infty \alpha(i\omega) d\omega, \quad (9)$$

where α is the polarisability, which gives a C^3 coefficient which agrees with experiment (e.g. [41]). This then yields [37]:

$$V_v(z) = 0.11 \frac{\hbar\Gamma}{k^3 z^3}, \quad (10)$$

with Γ being the natural linewidth of the dominant transition and k the associated wavevector. The dielectric constant for the nanowire chips to be used is not known, so the value for Silicon is used, which is the substrate for the nanowires, and is equal to 11.4 [42].

The inclusion of the Lennard-Jones potential does not make any discernable difference to the potential curves seen in Figure 11. The reason for this is that the van der Waals interaction does not overcome the energy shift due to the magnetic field until very close to the mirror, and this extremely short scale was not included in the computation. This region is of relatively little interest as the atom energy required to probe this region is considerably greater than is possible by dropping the atoms onto the chip; although there are ‘gaps’ in the potential due to the magnetic field (cf. Figure 12) to extract meaningful data about the system it would be desirable that the majority of atoms enter this attractive region. Further calculations could focus on the very short scale region in order to investigate at what distances adsorption of atoms could occur. However, these conclusions may be inaccurate due to the fact that the energy shifts due to the magnetic field are calculated according to the ‘monopole’ model - this must break down at very short distances as a divergent behaviour is unphysical. Further analysis using more rigorous micromagnetic simulations would be useful. It is possible to estimate the distance at which the magnetic potential and Lennard-Jones potential cancel. The $F = 2$, $m_F = 2$ stretched state responds to a magnetic field linearly with the simple relation $E = \mu_B B$. Inserting the expression for the magnetic field according to the monopole model (cf. Section 4.2) yields:

$$E = \frac{\mu_B q}{4\pi z^2}, \quad (11)$$

where q is the ‘magnetic charge’ parameter. Equating this to the expression for the Lennard-Jones potential given in Equation (10) gives the height at which the two cancel as:

$$z = 0.11 \frac{4\pi\hbar\Gamma}{\mu_B q k^3}, \quad (12)$$

which is equal to around 0.5 nm. This is very much lower

than previous atom mirror experiments, and is quite a surprising result in this sense. This is further emphasised when one considers the energy barrier of the potential that atoms must overcome to probe this regime. The potential takes the full form of

$$V = \frac{\mu_B q}{4\pi z^2} - 0.11 \frac{\hbar\lambda^3 \Gamma}{8\pi^3 z^3}. \quad (13)$$

Differentiating this and setting to zero yields

$$\frac{dV}{dz} = \frac{0.33\hbar\lambda^3 \Gamma}{8\pi^3 z^4} - \frac{\mu_B q}{2\pi z^3} = 0 \quad (14)$$

$$\Rightarrow z = \frac{0.33\hbar\lambda^3 \Gamma}{\mu_B q 4\pi^2} = 0.8 \text{ nm}. \quad (15)$$

Reinserting this value for z back into Equation (13) yields a potential of 8.36×10^{-22} J. Equating this to the gravitational potential energy of an atom above the nanowire substrate, mgh , gives a required drop height of 586 m in order to overcome this energy barrier.

Clearly this cannot be correct; the reason for this remarkably large value is that the monopole model of the magnetic field is a divergent one, and becomes increasingly inaccurate for decreasing distance from the domain wall. It assumes that the magnetic charge density is infinite, which is not the case. Thus, modelling of the potentials at short range would be greatly improved by more accurate simulations of the magnetic field, and comparisons between the monopole model and these more accurate simulations are ongoing to test the range over which the latter gives reasonable results. The remainder of this section will use magnetic fields created via micromagnetic simulations, rather than the monopole model.

Simulations of atoms bouncing from a nanowire-based mirror were carried out using a classical Monte Carlo simulation; interactions between the atoms are ignored, which is a good approximation given the low densities of atoms under consideration in a MOT.

The atoms are initially in a cloud with a Gaussian distribution of positions and a Maxwell-Boltzmann distribution of velocities. These initial conditions were randomly picked each time. This was done by mapping a random number (generated on the interval $[0,1]$) onto the relevant distribution function. The cumulative of that function has by definition a range which is also $[0,1]$. Hence, the inverse cumulative distribution function maps random numbers in this domain onto a range which is the distribution under consideration. For the case of components of atom velocity, their distributions are also Gaussian:

$$f(v_i) = \sqrt{\frac{m}{2\pi k_B T}} \exp\left(-\frac{mv_i^2}{2k_B T}\right), \quad (16)$$

where m is the atom mass, k_B is Boltzmann’s constant and T the temperature. The corresponding inverse cumulative distribution function is:

$$\Phi^{-1}(p) = \sqrt{\frac{2k_{\text{B}}T}{m}} \text{erf}^{-1}(2p - 1), \quad p \in [0, 1]. \quad (17)$$

The distribution of atom positions is completely analogous. The atoms were first modelled undergoing classical projectile motion and then simply being reflected from a flat surface. However, due to the periodic nature of the magnetic field produced by the array of domain walls, the potential experienced is a ‘corrugated’ one, so a simple reflection is an inaccurate one. A more accurate simulation is achieved by creating an effective isosurface from which the atoms bounce. It is seen in Equation (7) that a field of around 15 G is required in order to bounce Rubidium 87 atoms in the $m_{\text{F}} = 2$, $g_{\text{F}} = 1/2$ state. This field will be present at different heights across the array of nanowires, depending on the relative position of any domain walls. Figure 12 shows an effective isosurface at a constant 15.7 G [43].

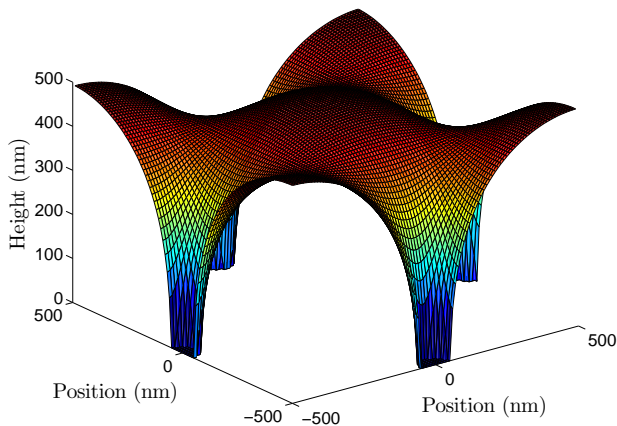


FIG. 12: A unit cell of the isosurface of constant magnetic field magnitude (chosen to be 15.7 G) due to an array of domain walls in magnetic nanowires.

This isosurface can then be considered as a physical surface from which the atoms bounce. This is still an approximation, as the reflection is being considered as a point interaction, occurring only at the surface. This is clearly not the case, but is a good approximation to make considering that the magnitude of the field decays rapidly away from the nanowires [14]. The reflection is then governed by the following simple formula:

$$\vec{v}' = \vec{v} - 2(\vec{v} \cdot \hat{n}) \hat{n}, \quad (18)$$

where \vec{v}' is the reflected velocity, \vec{v} is the incident velocity and \hat{n} is the normal vector of the surface at the point of reflection. \hat{n} is given by:

$$\hat{n} = \frac{\vec{x} \times \vec{y}}{|\vec{x} \times \vec{y}|}, \quad (19)$$

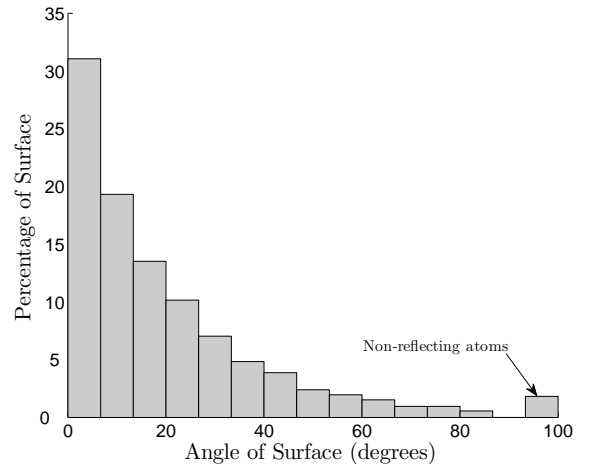


FIG. 13: A histogram showing the distribution of angles of the magnetic isosurface. All angles are relative to flat. The bin on the far right represents the proportion of the area of the chip that does not produce sufficient magnetic field to reflect atoms dropped from 1 cm.

where \vec{x} and \vec{y} are vectors tangential to the plane at the point of reflection and are easily found by differentiating the isosurface shown in Figure 12. It is found that the curvature of this isosurface makes a considerable difference to the behaviour of the system. Figure 13 shows quantitatively the nature of the surface in terms of the angle relative to flat.

As can be seen, there is a significant deviation from being flat over a sizeable proportion of the chip. There are also areas where the atoms will not be reflected as there is not a sufficiently large magnetic field. At these points one of two things can happen. Either the atoms will be attracted to the surface of the substrate by van der Waals interaction where they will ‘stick’, or they will undergo diffuse reflection from the substrate, although the latter is much less likely. The adsorption of Rubidium by the substrate should not be a problem, as the number of atoms which do so will be negligible, and the functionality of the mirror is not critically dependent on its physical flatness.

With this simulation it is then possible to track how the atoms evolve in time. However, the more important consideration is the signal that will be extracted from the experiment proper. It is planned that a light sheet resonant on the $F = 2$ to $F = 3$ transition will be used in order to observe the atoms, in a similar manner to previous work [44, 45]. The doppler shift due to the component of the atomic velocity along the light sheet will have negligible effect on the signal extracted. The atoms will spend under a millisecond in the light sheet, so the use of repump light should not be necessary. Analysis of the number of atoms bouncing may also be done by a ‘release and capture’ method, as in e.g. [46]. Predictions of the signal extracted from the system were possible by analysing the total number of atoms within such a light sheet as a function of time. Figure 14 shows the predictions for such a signal. It is assumed that the atoms are

dropped from a height of 1 cm and the light sheet has a width of 15 mm and a thickness of 0.2 mm, and is at a height of 4.5 mm. The initial size of the cloud of atoms is defined as having 3 standard deviations of all the atoms contained within a radius of 1 mm.

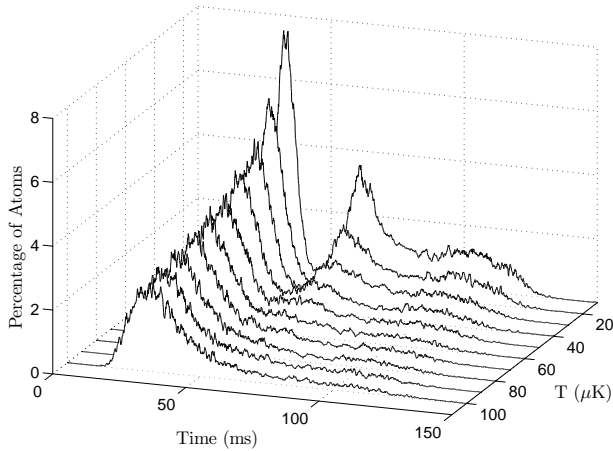


FIG. 14: The simulated signal from a light sheet placed above the nanowire mirror as a function of temperature, T . The sheet is 4.5 mm above the substrate and the atoms are dropped from 1 cm.

For lower temperatures, there are two clearly discernable peaks, corresponding to the cloud of atoms initially falling through the light sheet, and then being reflected and passing through again. It is only just possible to resolve separate peaks for the reflected cloud's passages upwards and downwards through the light sheet. This is because by the time it has been reflected, the velocity spread of the atoms means that they are spatially spread out and the cloud is less defined. The parameters chosen try to optimise this resolution at lower temperatures, but are less favourable at higher temperatures. There is limited improvement seen by further cooling due to the initial spatial spread of the atoms. To better resolve the features the parameters must be chosen carefully. Clearly, a small cloud of atoms will improve the resolution, as will a larger drop height or a smaller distance between the light sheet and the substrate. However, moving the light sheet down becomes a trade off, as the closer it is the more difficult it is to distinguish between the signal from the initial fall and subsequent bounce. Thus the simulation is a useful tool in optimising how the experiment is to be set up, whilst taking into consideration other factors such as the positioning of other equipment, e.g. coils inside the chamber. It also shows well the fact that altering these parameters will alter the size of the signal as well as its width.

As the temperature increases, this effect of 'smearing' the signal becomes more pronounced - the peaks become much less sharp. The height of the peaks also becomes less for higher temperatures, as more atoms miss the chip altogether and aren't reflected. The clarity of the peaks seen in this signal is not as good as in similar previous work such as [44]. This is most likely to be due to the fact

that the magnetic field created is quite 'rough' compared to other atom mirrors which use ferromagnetic thin films. This is because of the pattern of magnetisation produced - the 2D array of domain walls is quite different to the ideal sinusoidal magnetisation pattern. This is accentuated by the small scale of the nanowires - there is a higher field gradient and atoms are reflected closer to the surface where the corrugation effect is more pronounced.

4. MOBILE ATOM TRAP

The second main experiment that will be carried out with magnetic nanowires is that of a tightly confining mobile atom trap. In contrast to the magnetic mirror experiment, which requires a large number of domain walls and the field produced by them, this experiment is based around a single domain wall. In this sense it is a more microscopic regime. Figure 15 shows the magnetic field created by a single nanowire domain wall.

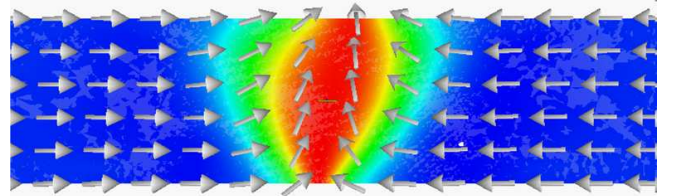


FIG. 15: Qualitative illustration of the magnetisation created within a single domain wall [47]. The arrows show the direction of the magnetisation, and the colour shows the magnitude of the magnetisation in the longitudinal direction.

The domain wall illustrated is a transverse one. It is also possible to create vortex type domain walls, which are more often found in wider, thicker domain walls.

The important aspect of this experiment is to create a suitable magnetic trapping potential. It has already been said that the magnetic field produced by the nanowires falls off rapidly with increasing distance (the field is modelled well by a $|\vec{B}| \sim 1/r^2$ relation, particularly at larger distance). In order to create a potential which is confining for a weak field seeking state a bias field is required. This creates a magnetic field minimum at a height determined by the bias field strength. The field produced by a single domain wall and a bias field is very similar to a quadrupole trap for small scales around the minimum, which has the familiar form:

$$\vec{B}_{\text{quad}} = B' \left(\frac{x}{2} \hat{x} + \frac{y}{2} \hat{y} - z \hat{z} \right). \quad (20)$$

The problem with this potential form is that it has a zero point. Atoms which pass through or close to this point can undergo non-adiabatic Majorana spin flip transitions into an untrapped magnetic sublevel, leading to their loss [48]. This can be derived in terms of the general quantum mechanics adiabaticity approximation [49]:

$$\frac{1}{\hbar\omega_{mn}} \left\langle \phi_m(t) \left| \frac{\partial \hat{H}(t)}{\partial t} \right| \phi_n(t) \right\rangle \ll \omega_{mn}, \quad (21)$$

where $\phi_{m,n}$ are instantaneous eigenstates and ω_{mn} is the associated transition frequency. For the case of magnetic spin flips, ω_{mn} is equal to ω_L and $H(t) = \mu B$, giving:

$$\frac{1}{\mu B} \cdot \mu \frac{\partial B}{\partial t} = \frac{1}{|\vec{B}|} \frac{\partial B}{\partial t} \ll \omega_L. \quad (22)$$

Thus, if an atom travels slowly enough in the vicinity of a zero point (where this Larmor frequency vanishes) then such a spin flip transition is likely to happen. The atom can end up in a strong field seeking state and subsequently be lost from the system.

To circumvent this, the minimum of the trap should be non-zero. This can be achieved in a number of different ways, for example a Ioffe-Pritchard trap consists in its

most familiar form of two Helmholtz coils and four wires of current. However, this type of trap is not suitable for implementation in this experiment (for more detail see Section B). A couple of methods have been considered to create a suitable potential.

4.1. TOP Traps

Time Orbiting Potentials are formed by adding in a time varying magnetic field of the following form to a static magnetic potential:

$$\vec{B}_{\text{TOP}}(t) = B_0 [\cos(\omega_T t) \hat{x} + \sin(\omega_T t) \hat{y}] \quad (23)$$

It is assumed that the magnetic dipoles of the trapped atoms follow the magnetic field. Under this assumption, the additional time varying field gives rise to the following potential:

$$U(\vec{r}, t) = \mu \left| \vec{B}_{\text{quad}} + \vec{B}_{\text{TOP}} \right| = \mu \sqrt{\left[\frac{B'}{2}x + B_0 \cos(\omega_T t) \right]^2 + \left[\frac{B'}{2}y + B_0 \sin(\omega_T t) \right]^2 + (B'z)^2}. \quad (24)$$

The effective potential that is experienced by atoms in a TOP trap is given by the time averaged value. Also included is the potential due to gravity, although the effect this has is very small. Evaluating this and Taylor expanding gives the following expression [50]:

$$\begin{aligned} U(\vec{r}) &= \frac{1}{2\pi} \int_0^{2\pi} U(\vec{r}, t) dt + mgz \\ &= mgz + \mu B_0 + \frac{\mu B'^2}{16B_0} (x^2 + y^2) + \frac{\mu B'^2}{2B_0} z^2 + \dots \end{aligned} \quad (25)$$

The most important thing which is immediately obvious is that there is a non-zero minimum which occurs at (0,0,0) and is equal to μB_0 . If one was to consider the TOP trap in greater detail aspects such as including the gravitational potential and the resulting anharmonicity of the trap would be important. However, it was decided that the TOP trap would not be a suitable option for this experiment.

There are a couple of reasons why an alternative to the TOP trap was sought. Firstly, it would be particularly difficult to implement the TOP trap within the experimental setup. Two sets of coils are required to produce the necessary time varying field. These have to be accurately phase locked and inductance matched. These coils would then have to be either placed outside the chamber with a very large current passing through them, or smaller and placed inside the vacuum chamber. It is believed that either option would prove to be logistically and technically very demanding.

There is a more fundamental reason why it would not be possible to use a TOP trap scheme. There are a couple of conditions which must be met in order for a Time Orbiting Potential to form an effective trapping potential (see e.g. [50, 51]). The first of these is the time averaging condition. The frequency of the time varying field must be sufficiently high such that the assumption that the atoms only 'see' the time averaged potential is valid. There is always a zero point within the potential, which precesses in a 'circle of death' - any atoms which spend a long enough time in the vicinity of this zero point may undergo a non-adiabatic spin flip. The time spent around a zero point is governed by the trap frequency, ω (to a good approximation, that of the static potential). Thus the frequency of oscillation of the field must be significantly greater than the trap frequency, and the time averaging condition can be written as [50, 52]:

$$\omega_T \gg \omega. \quad (26)$$

The second condition that is necessary for an effective TOP trap is that of adiabaticity. It is assumed that the degree of freedom associated with the angular momentum of the atom is rigidly coupled to the translational and rotational freedom of the atom [53]. This is true if the atom follows the potential adiabatically. If the trap's potential varies too quickly, the atom will not be able to 'keep up' with this variation. The timescale over which an atom can follow such a potential is quantified by the Larmor frequency, ω_L , which has to be significantly larger

than the frequency of oscillation of the field [50]:

$$\omega_L \gg \omega_T. \quad (27)$$

Considering the fields produced from the nanowires it quickly becomes evident that a TOP trap is not a viable option, due to the fact that both the Larmor frequency and the trap frequency depend on the magnitude of the magnetic field. It has been calculated that trap frequencies of around 160 kHz are expected for the potential due to a single domain wall [14]. The Larmor frequency is given by $\omega_L = \frac{m_F g_F \mu_B B}{\hbar}$ [54], and is expected to be around 5000 kHz. It is clear that Equations (26) and (27) can not be simultaneously satisfied given these values. Thus it seems that a TOP trap would be truly infeasible for this application.

4.2. RF Dressing

Due to the infeasibility of a TOP scheme, it is hoped that RF dressing can be used to create a suitable trapping potential instead. RF dressing and TOP traps are essentially two aspects of the same phenomenon - the addition of a time varying field to a static field. In the case of a TOP trap, the modification is a perturbative one, whilst for RF dressing the frequencies involved are much higher and it is no longer perturbative; one must consider the energy levels as being dressed by the extra field.

In an RF dressed trap an external field of the form $\vec{B}_0 \cos(\omega_{\text{rf}} t)$ is applied, and there are two associated frequencies. The first is ω_{rf} which is the frequency at which the field varies in time, just as with a TOP trap. The larger this frequency is the more the energy levels of the static trap are shifted. With a sufficiently high frequency, the energy levels will ‘overlap’, which must lead to avoided crossings [55]. The other frequency to consider is an effective Rabi frequency, Ω , which is given by Equation (28):

$$\Omega = \frac{\vec{\mu} \cdot \vec{B}_0}{\hbar} = \frac{m_F g_F \mu_B B}{\hbar}, \quad (28)$$

(an alternative formulation is offered in [56], but the final result is essentially equivalent). This is a measure of the amount of ‘mixing’ of the states. The higher the applied magnetic field amplitude, the more the static potentials are dressed.

The theory regarding the resulting potentials from RF dressing a static magnetic field is covered in much greater detail elsewhere [57, 58], and descriptions of successful implementations are well documented (e.g. [59–61]). The theoretical background shall not be discussed here. Instead, a ‘master formula’ is quoted, from which it is possible to analyse the expected resulting potentials [62]. As with the case of a TOP trap, the potential due to gravity has also been included for completeness but has negligible effect:

$$U(\vec{r}) = m_F g_F \mu_B \sqrt{\left(\left| \vec{B}_S(\vec{r}) \right| - \frac{\hbar \omega_{\text{rf}}}{g_F \mu_B} \right)^2 + \frac{1}{4} \left| \hat{e}_S \times \sum_i \vec{B}_{\text{rf}}^i(\vec{r}) \right|^2} + mgz, \quad (29)$$

where it is assumed that the RF field is a linearly polarised one. The first term in Equation (29), $\left| \vec{B}_S(\vec{r}) \right|$, corresponds to the static field - the field that is present before any dressing takes place. The next term, $\frac{\hbar \omega_{\text{rf}}}{g_F \mu_B}$, is the shift in energy levels caused by the RF field. The final term, represents the dressing of the energy levels by the RF field. In general one can have any number, i , of RF fields, but for current applications within this project 1 is sufficient. As can be seen, the ‘mixing’ of the fields is more pronounced when the dressing field is perpendicular to the static field. Through a judicious choice of parameters it is possible to change the shape and depth of the potential that is formed - both single and double wells are possible with one dressing field.

It is a fairly simple matter to find the resulting potentials once the form of the static field and the RF field are known. It is a good approximation to consider the RF fields as being homogenous, as they are just produced by a pair of coils, but a more rigorous treatment is provided in Section B. The nature of the field produced by the

nanowire domain walls is one of the most interesting features of the experiment, and it is vital to its efficacy. It is currently the subject of analysis. Micromagnetic simulations are carried out by colleagues at the Engineering Materials department of the University of Sheffield to give the nature of the magnetisation of the nanowires. This is carried out using the Landau-Lifshitz-Gilbert equation of motion and quasistatic Maxwell equations, solved using a finite element/boundary element method [63]. This is a time consuming and laborious process, so a simpler model is desired. This is provided by a ‘monopole’ model [43]. The domain wall is approximated as being a pole from which magnetic field lines emanate. A direct analogy is made with Coulomb’s law in electrostatics, and the magnetic scalar potential, ϕ_m , is given by:

$$\phi_m = \frac{q_m}{4\pi\mu_0 r}, \quad (30)$$

and thus the magnetising field, H is given by:

$$H = -\vec{\nabla}\phi_m = \frac{q_m}{4\pi\mu_0 r^2}, \quad (31)$$

and the magnetic field, B , is given by $\mu_0 H$. In analogy with Gauss' law:

$$\vec{\nabla}\cdot\vec{H} = \frac{\rho_m}{\mu_0}. \quad (32)$$

Equivalently for magnetism

$$\vec{\nabla}\cdot\vec{B} = 0, \quad (33)$$

which in the presence of a magnetising medium is equivalent to

$$\mu_0\vec{\nabla}\cdot(\vec{H} + \vec{M}) = 0 \quad (34)$$

$$\Rightarrow \vec{\nabla}\cdot\vec{H} = -\vec{\nabla}\cdot\vec{M}. \quad (35)$$

Substituting in Equation (32) then yields:

$$\rho_m = -\mu_0\vec{\nabla}\cdot\vec{M}, \quad (36)$$

recasting Equation (30) for a continuous 'magnetic charge' distribution gives the potential at a point \vec{r}_0 :

$$\phi(\vec{r}_0) = \int \frac{\rho_m(\vec{r}) dV}{4\pi\mu_0 |\vec{r}_0 - \vec{r}|}. \quad (37)$$

Assuming that the charge distribution is well characterised by a monopole one can replace $\rho_m(\vec{r})$ with $\vec{\nabla}\cdot\vec{M}$ and $|\vec{r}_0 - \vec{r}|$ becomes simply r , the distance from the monopole to \vec{r}_0 :

$$\phi(r) = -\frac{\int \vec{\nabla}\cdot\vec{M} dV}{4\pi\mu_0 r}. \quad (38)$$

Comparing this with Equation (30) gives an expression for the 'magnetic charge':

$$q_m = -\mu_0 \int \vec{\nabla}\cdot\vec{M} dV. \quad (39)$$

Employing the divergence theorem then yields:

$$q_m = -\mu_0 \int \vec{M}\cdot\hat{n} dS, \quad (40)$$

where \hat{n} is the normal vector of the surface encompassing the magnetic charge. Clearly, the case under consideration is that of a domain wall, and it is assumed that all the magnetic charge is contained in this wall. Thus, the surface encompassing the charge has length w , the width

of the nanowire, depth t , the thickness of the wire, and a vanishing width, reducing Equation (40) to:

$$q_m = 2\mu_0 w t M, \quad (41)$$

where M is the magnetisation as previously defined, which can also be considered as the magnetic moment density, which is $\sim 8 \times 10^5$ A/m for permalloy [43, 64].

With the field from the domain wall known it is relatively easy to then use Equation (29) to find the resultant field and potential. To recap, a domain wall creates a field rapidly decaying ($1/r^2$) from the nanowire surface, then adding a bias field produces a trapping field with a zero point. RF dressing this field with another field of the form $B_0 \cos(\omega_{rf}t)$ removes the zero point to produce a potential which is suitable for stable trapping of atoms in a weak field seeking state. This progression is illustrated in Figure 16. The bias field is chosen so as to create a minimum at a height of 500 nm. The data show good agreement with that in previous work [14].

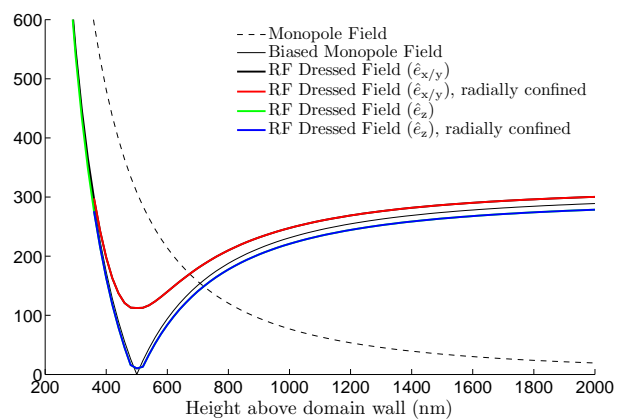


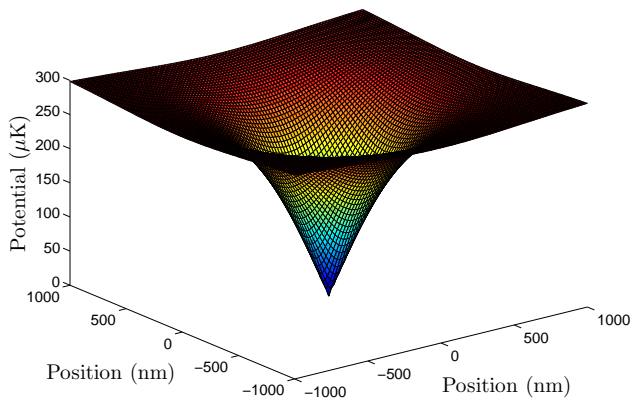
FIG. 16: Plot of the potential directly above a domain wall as a function of height, z . The RF dressing is applied with $B_0 = 5$ G and $\omega_{rf} = 100$ kHz. The nanowire geometry used is a width of 200 nm and a thickness of 5 nm, which yields a charge constant, q , of 2.16×10^{-15} Tm. The atom energy is defined as $E = 3/2k_B T$.

The shape of the field in the x and y directions is illustrated in Figure 17. At the height of the field minimum the radial character reduces to a linear one as the z component of field essentially disappears across all x and y ; the z component of the field does not vary by an appreciable amount across this range. Moving away from this height the field magnitude varies quadratically across x and y .

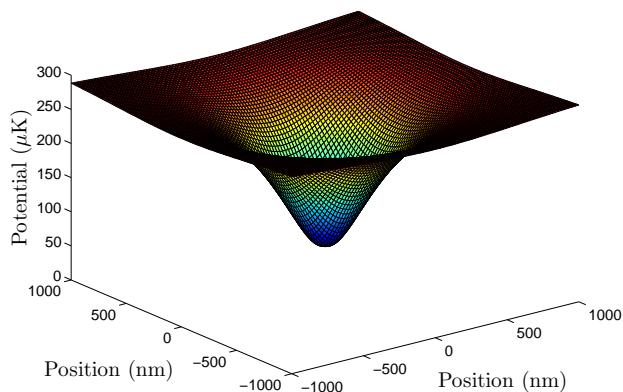
With the parameters named (cf. Figure 16) one can see that the depth of the undressed (dressed) trap is around $300 \mu\text{K}$ ($220 \mu\text{K}$) in both the axial and radial directions. The effective potential, V is related to the magnetic field by

$$V = m_{FGF}\mu_B|\vec{B}|. \quad (42)$$

Equating this energy with the kinetic energy, E , of a gas



(a) Radial plot of the potential at a height of 500 nm with no RF dressing.



(b) The potential given above, now dressed by a RF field of the form $B_0 \cos(\omega_{rf}t)$, with $B_0 = 3$ G and $\omega_{rf} = 1$ MHz.

FIG. 17: The radial field due to a single domain wall and a bias field at a height of 500 nm and the effect of then dressing this field with an RF field.

one can evaluate the effective trap depth in Kelvin:

$$E = 3/2k_B T$$

$$\Rightarrow T = \frac{2m_F g_F \mu_B |\vec{B}|}{3k_B}. \quad (43)$$

5. OUTLOOK

The immediate goal within the project is to achieve and characterise a MOT in the new Kimball chamber (Figure 18). Initial setup is being carried out with external coils. Work is also being done to finalise the design of the coils and mount that will go into the chamber. Once this is completed it will be necessary to make these and rebake the chamber with them in place. The first atom mirror experiments may then begin.

Quantitative analysis of the atom trapping potential continues and it is hoped that a consensus will be drawn

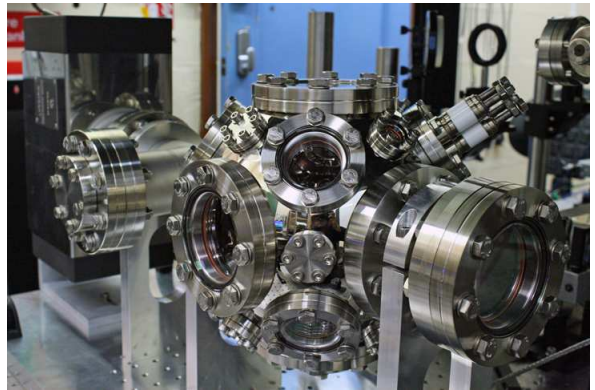


FIG. 18: The chamber in which the nanowire experiments will be carried out - a Kimball Physics expanded spherical cube with a Varian Starcell 20 litre ion pump.

as to what the optimum wire geometry will be for the mobile atom trap experiment, as well as how accurate the monopole model is through comparison with the micromagnetic simulations.

APPENDIX A: POLARISATION SPECTROSCOPY

Polarisation spectroscopy is a form of pump probe spectroscopy that relies on an induced dichroism within the atomic vapour to create an error signal suitable for locking to. A diagram illustrating a typical polarisation spectroscopy setup is shown in Figure 19.

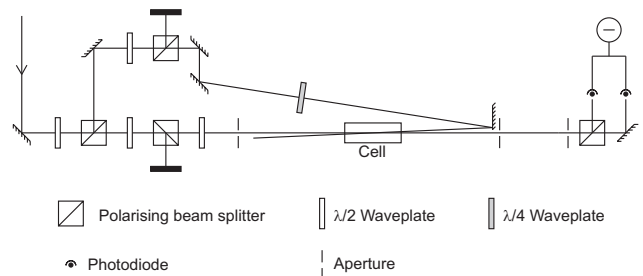


FIG. 19: Experimental setup for polarisation spectroscopy. The signal is analysed using a differential photodiode.

Polarisation spectroscopy is a well documented technique and the interested reader can find more thorough discussions in e.g. [65–67]. A linearly polarised weak probe beam interrogates the vapour cell whilst a circularly polarised pump beam counterpropagates through the cell. All mirrors used in the setup are dielectric ones, except for that which reflects the pump beam into the vapour cell, which is metal. The reason for this is that dielectric mirrors have a higher reflectivity ($\sim 99\%$) than metal mirrors ($\sim 95\%$), yet do not perfectly preserve polarisation. For most cases, reflectivity is paramount, but the probe beam should be as close to circularly polarised as possible for optimum efficiency. Thus a metal mirror is chosen in order to do this. The experimental setup shown also includes waveplates and polarising beam split-

ters which allow for independent control of the pump and probe beam intensities. As with all doppler free pump-probe spectroscopy, efforts are made to ensure pump and probe are as close to counterpropagating as possible.

The circularly polarised probe beam pumps σ transitions. This is what induces the dichroism within the medium; atoms pumped into states with higher values of $|m_F|$ are more likely to subsequently undergo σ transitions of a particular sign (either σ^+ or σ^-). This is illustrated by Figure 20, which shows the relative strength of the possible transitions between the $5^2S_{1/2}$, $F = 2$ and $5^2P_{3/2}$, $F = 3$ states.

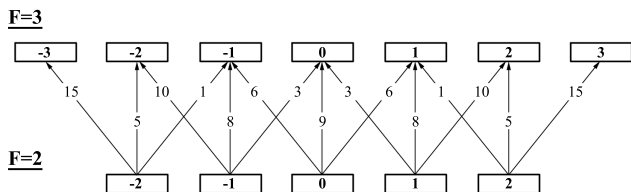


FIG. 20: Rescaled Clebsch-Gordan coefficients for transitions on the Rubidium 87 D2 line. The numbers inside the boxes are the m_F values.

For example, if an atom is pumped into the $F = 2$, $m_F = 2$ state by σ^+ transitions, it is then 15 times more likely to undergo another σ^+ transition than a σ^- one.

The vapour cell is probed by light which is linearly polarised (usually at 45°). This can be considered as a superposition of right and left handed circularly polarised light. The electric field of the probe beam is given by:

$$\vec{E} = E_x \hat{x} + E_y \hat{y} = E_0 (\cos \phi \hat{x} + \sin \phi \hat{y}) \quad (\text{A1})$$

$$= \frac{E_0}{2} [e^{-i\phi} (\hat{x} + i\hat{y}) + e^{i\phi} (\hat{x} - i\hat{y})]. \quad (\text{A2})$$

Because of the optical pumping, the left and right handed components will experience different absorption coefficients, yielding:

$$\vec{E} = E_0 \exp\left(ik_+L - \frac{\alpha_+L}{2}\right) \frac{\exp(-i\phi)}{2} (\hat{x} + i\hat{y}) + E_0 \exp\left(ik_-L - \frac{\alpha_-L}{2}\right) \frac{\exp(i\phi)}{2} (\hat{x} - i\hat{y}), \quad (\text{A3})$$

where L is the length of the cell, α_{\pm} are the absorption coefficients corresponding to σ^{\pm} transitions, and k_{\pm} are the wavevectors ($k_{\pm} = \frac{\omega}{c}n_{\pm}$ with n the refractive index). Thus, as the probe light passes through the vapour cell, the different components are absorbed and refracted by different amounts. After the vapour cell, the light gets decomposed back into horizontal and vertical components, and the output intensity is given by:

$$\begin{aligned} I &= E_x^2 - E_y^2 \\ &= -\frac{\varepsilon_0 c E_0^2}{2} \exp\left[-\frac{(\alpha_+ + \alpha_-)L}{2}\right] \cos(2\phi + 2\Phi) \\ &= -I_0 \cos(2\phi + 2\Phi), \end{aligned} \quad (\text{A4})$$

where Φ is defined as $\frac{\pi(n_+ - n_-)L}{\lambda}$, and ϕ is the initial angle of linear polarisation. ϕ is usually chosen to be 45° as this gives the greatest sensitivity to Φ (the differential of \cos is maximal at $\pi/2$).

The absorption coefficients are dependent on the detuning, and are given by the familiar Lorentzian. Thus the difference between α_+ and α_- , denoted $\delta\alpha$ is given by:

$$\delta\alpha = \frac{\delta\alpha_0}{1 + 4\Delta^2/\Gamma^2}, \quad (\text{A5})$$

where Δ is the detuning, Γ is the natural linewidth, and α_0 is the absorption coefficient on resonance, which can be calculated taking into account the distribution of population among the m_F sublevels. There is then a concomitantly defined refractive index, which is given by a Kramers-Kronig relation:

$$n(\omega) = 1 + \frac{c}{\pi} PV \int_0^\infty \frac{\alpha(\omega')}{\omega'^2 - \omega^2} d\omega', \quad (\text{A6})$$

which then implies:

$$\delta n = \delta n_0 \frac{2c}{\omega_0 \Gamma} \frac{\Delta}{1 + 4\Delta^2/\Gamma^2}. \quad (\text{A7})$$

It is now possible to calculate the output intensity for any combination of physical parameters, with a given population distribution within the set of m_F sublevels. Analysis of this population distribution behaviour is beyond the scope of this work.

A theoretical lineshape from a polarisation spectroscopy setup is shown in Figure 21. As can be seen,

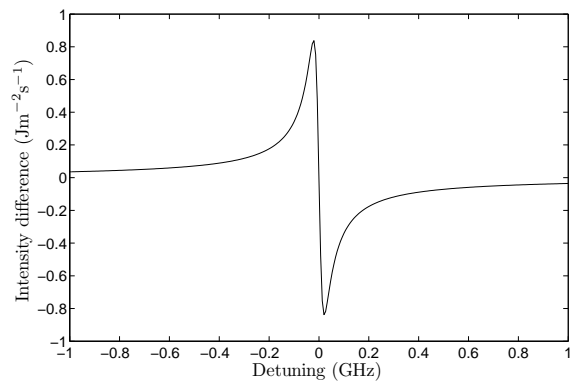


FIG. 21: A theoretical polarisation spectroscopy signal for a single Rubidium 87 D2 line transition.

the lineshape is an ideal one for laser locking, as it has a steep gradient and clear zero crossing. The shape shown in Figure 21 is physically unrealistic, as real atoms contain a large number of different transitions, each with its own resonance, whereas the shape shown here is that associated with just one resonance.

Because of the stimulated dichroism and concomitant birefringence of the medium, the vapour cell causes a rotation and induced ellipticity of the polarisation of the probe beam. This can be explicitly analysed by considering again Equation A1 and adding in explicit spatial (along beam axis) and time dependence:

$$E = E_0 [\cos(kz - \omega t) \cos \phi \hat{x} + \cos(kz - \omega t) \sin \phi \hat{y}]. \quad (\text{A8})$$

$$E = \frac{E_0}{\sqrt{2}} \{ [\sin(k_+z - \omega t + \phi) \hat{x} + \cos(k_+z - \omega t + \phi) \hat{y}] e^{-\alpha_+L} - [\sin(k_-z - \omega t - \phi) \hat{x} - \cos(k_-z - \omega t - \phi) \hat{y}] e^{-\alpha_-L} \}. \quad (\text{A10})$$

Resolving into horizontal and vertical components gives two expressions for the time evolution of the electric field, which allows for direct analysis of the rotation and ellipticity of the probe beam. It is expected that the induced polarisation rotation will only be of the order of 2 degrees, and the ellipticity will be similarly very small.

One way to enhance the effects observed would be to heat the vapour cell. This would provide a greater number density of atoms, and would in turn induce a much larger polarisation. It is even thought that at sufficiently high temperatures the lineshape will produce a new feature, which is shown in Figure 22:

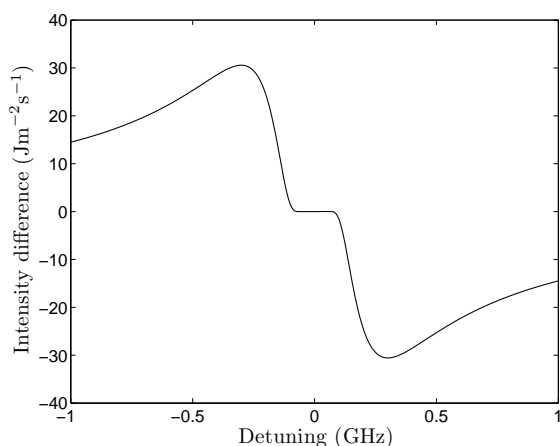


FIG. 22: A predicted lineshape from polarisation spectroscopy carried out on Rubidium 87 at a temperature of 380 K. The zero crossing is no longer smooth as Φ is rotated through an angle of greater than π .

The electric field oscillates in time along a path defined by the polarisation. Decomposing the above expression into a basis of left and right handedness in a purely real manner gives:

$$E = \frac{E_0}{\sqrt{2}} [\sin(kz - \omega t + \phi) \hat{x} + \cos(kz - \omega t + \phi) \hat{y}] \quad (\text{A9})$$

$$- \frac{E_0}{\sqrt{2}} [\sin(kz - \omega t - \phi) \hat{x} - \cos(kz - \omega t - \phi) \hat{y}].$$

Adding in parity dependent refraction and absorption:

APPENDIX B: IOFFE-PRITCHARD TRAP

The Ioffe-Pritchard trap has become a very useful tool within atomic physics since its first demonstration in 1983 [68], based on an earlier proposal for plasma confinement [69]. It provides a stable magnetic trap for atoms with a non-zero minimum which helps prevent spin flips. This section will analyse the nature of the field produced by the trap, which will in turn relate the types of magnetic field to real life parameters, allowing for the synthesis of fields of particular gradient or curvature.

The Ioffe-Pritchard trap in its most common form consists of a two coils in Helmholtz configuration (current flowing in same sense) and a set of 4 wires with current flowing in alternating direction, as shown in Figure 23.

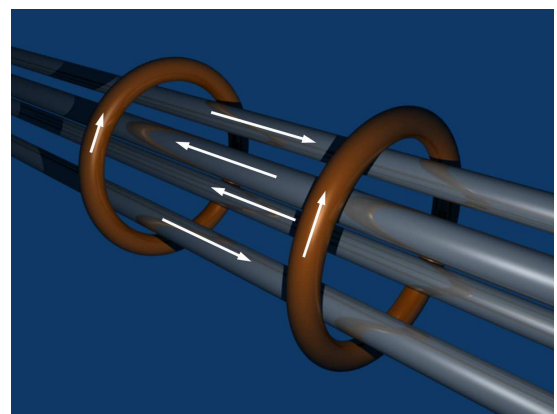


FIG. 23: A diagram of a Ioffe-Pritchard trap, consisting of 2 Helmholtz coils and 4 wires. The arrows represent the direction of flow of current

The form of the magnetic field produced by this arrangement is given in Equation (B1) [70]:

$$\vec{B} = B_0 \begin{pmatrix} 0 \\ 0 \\ 1 \end{pmatrix} + B' \begin{pmatrix} x \\ -y \\ 0 \end{pmatrix} + \frac{B''}{2} \begin{pmatrix} -xz \\ -yz \\ z^2 - \frac{1}{2}(x^2 + y^2) \end{pmatrix}. \quad (\text{B1})$$

The magnetic field form is divided into 3 components - the bias, the gradient and the curvature. To a good approximation, the coils provide the bias and curvature alone, whilst the 4 wires provide a field gradient.

Considering the coils on their own, the field produced from such a configuration on axis is given by Equation B2 [71] (one needs only consider the field on axis for atom trapping purposes, as that is where any trapped sample will reside).

$$\vec{B} = \frac{\mu_0 I a^2}{2} \left[\frac{1}{(a^2 + x^2)^{3/2}} + \frac{1}{(a^2 + (L-x)^2)^{3/2}} \right] \hat{k}, \quad (\text{B2})$$

where I is the current flowing through the coils, a is the radius of both coils, L is their separation, x is the distance on axis from the centre of one of the coils and \hat{k} is the normal vector pointing along axis in the correct 'right hand' sense. Taking this expression and Taylor expanding it around $L/2$ (halfway between the coils - where the atoms will be) gives the following expression:

$$B(x) = B(L/2) + B'(L/2)(x - L/2) + \frac{B''(L/2)}{2}(x - L/2)^2 + \dots \quad (\text{B3})$$

As expected, the second term is zero, and the bias constant, B_0 and curvature constant B'' (cf. Equation (B2)) are given by:

$$B_0 = \frac{\mu_0 I a^2}{(a^2 + L^2/4)^{3/2}} \quad (\text{B4})$$

$$B'' = \frac{15L^2 \mu_0 I a^2}{8(a^2 + L^2/4)^{7/2}} - \frac{3\mu_0 I a^2}{2(a^2 + L^2/4)^{5/2}}. \quad (\text{B5})$$

The case under consideration here is on axis, meaning $x = 0, y = 0$ in the final term of Equation (B1), but since B'' is a common prefactor there is no loss of generality.

Similar analysis can be carried out for the 4 wires in the setup. The field created from them is of a quadrupole form and has no bias or curvature terms. It is illustrated in Figure 24.

The field from a single long current carrying wire is given by the well known Biot-Savart law:

$$\vec{B} = \frac{\mu_0 I}{2\pi R} \hat{\phi}, \quad (\text{B6})$$

where $\hat{\phi}$ is a unit vector in the azimuthal direction. From this one can write the field at any point from the 4 wires. The y component is given by Equation (B7) and there is

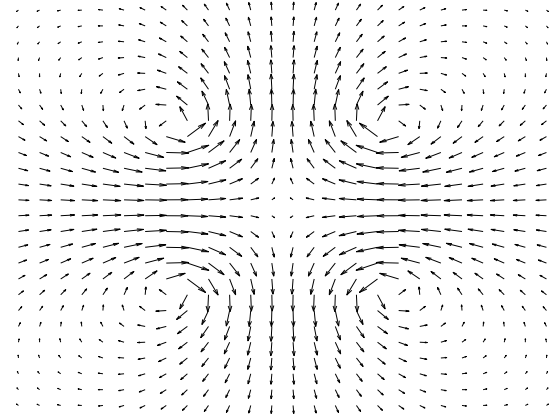


FIG. 24: Illustration of the quadrupole field created by 4 wires with the current direction alternating between adjacent wires.

an entirely analogous expression for the x component.

$$\sum_{i,j} \frac{\mu_0}{2\pi} \frac{\cos\left(\tan^{-1}\left(\frac{A_i}{B_j}\right)\right)}{\sqrt{A_i^2 + B_j^2}}, \quad (\text{B7})$$

where $\{A_i\} = \{y \pm d\}, \{B_j\} = \{x \pm d\}$ and the length of the square formed by the wire positions is $2d$. Taylor expanding this expression and assuming that $x \rightarrow 0$ as well, (valid since atoms will be found only at the middle of the wires), yields a zeroth order term equal to zero, and a gradient term given by:

$$B' = \frac{\mu_0 I}{\pi d^2}, \quad (\text{B8})$$

which is in agreement with previous work [72]. With these expressions it is then possible to judge the physical parameters required to create a given field bias, gradient and curvature.

-
- [1] S. Chu, Rev. Mod. Phys. **70**, 685 (1998).
 [2] E. L. Raab, M. Prentiss, A. Cable, S. Chu, and D. E. Pritchard, Phys. Rev. Lett. **59**, 2631 (1987).
 [3] M. Singh, R. McLean, A. Sidorov, and P. Hannaford, Phys. Rev. A **79**, 053407 (2009).
 [4] A. Günther, S. Kraft, M. Kemmler, D. Koelle, R. Kleiner,

- C. Zimmermann, and J. Fortágh, Phys. Rev. Lett. **95**, 170405 (2005).
 [5] J. Fortágh and C. Zimmerman, Reviews of Modern Physics **79**, 235 (2007).
 [6] T. Kishimoto, H. Hachisu, J. Fujiki, K. Nagato, M. Yasuda, and H. Katori, Phys. Rev. Lett. **96**, 123001 (2006).

- [7] S. Schlunk, A. Marian, W. Schöllkopf, and G. Meijer, Phys. Rev. A **77**, 043408 (2008).
- [8] D. D. Yavuz, N. A. Proite, and J. T. Green, Phys. Rev. A **79**, 055401 (2009).
- [9] A. Ruschhaupt, A. del Campo, and J. G. Muga, Phys. Rev. A **79**, 023616 (2009).
- [10] B. Vaucher, S. J. Thwaite, and D. Jaksch, Phys. Rev. A **78**, 043415 (2008).
- [11] R. P. Bertram, H. Merimeche, M. Mützel, H. Metcalf, D. Haubrich, D. Mesched, P. Rosenbusch, and E. A. Hinds, Phys. Rev. A **63**, 053405 (2001).
- [12] M. Metsälä, J. J. Gilijamse, S. Hoekstra, S. Y. T. van de Meerakker, and G. Meijer, New Journal of Physics **10**, 053018 (2008).
- [13] A. K. Mohapatra and C. S. Unnikrishnan, Europhys. Lett. **73**, 839 (2006).
- [14] D. A. Allwood, T. Schreffl, G. Hrkac, I. G. Hughes, and C. S. Adams, Applied Physics Letters **89**, 014102 (2006).
- [15] D. A. Allwood, G. Xiong, C. C. Faulkner, D. Atkinson, D. Petit, and R. P. Cowburn, Science **309**, 1688 (2005).
- [16] A. Himeno, T. Ono, and S. Nasu, J. Appl. Phys. **93**, 8430 (2003).
- [17] I. M. Watt, J. Phys. E **19**, 090668 (1986).
- [18] M. R. Scheinfein, J. Unguris, M. H. Kelley, D. T. Pierce, and R. J. Celotta, Rev. Sci. Instrum. **61**, 2501 (1990).
- [19] A. D. L. Humphris, M. J. Miles, and Hobbs, Appl. Phys. Lett. **86**, 034106 (2005).
- [20] Z. Q. Qiu and S. D. Bader, Rev. Sci. Instr. **71**, 1243 (2000).
- [21] Y. Martin and H. K. Wickramasinghe, Appl. Phys. Lett. **50**, 1455 (1987).
- [22] T. G. Sorop, C. Untiedt, F. Luis, and L. J. de Jongh, J. Appl. Phys. **93**, 7044 (2003).
- [23] A. M. Chang, H. D. Hallen, L. Harriott, H. F. Hess, H. L. Kao, J. Kwo, R. E. Miller, R. Wolfe, J. van der Ziel, and T. Y. Chang, Appl. Phys. Lett. **61**, 1974 (1992).
- [24] V. V. Khotkevych, M. V. Milošević, and S. J. Bending, Rev. Sci. Instr. **79**, 123708 (2008).
- [25] D. A. Steck, *Rubidium 87 d line data*, available online at <http://steck.us/alkalidata> (2001).
- [26] C. J. Foot, *Atomic Physics* (Oxford, 2005).
- [27] S. Gasiorowicz, *Quantum Physics* (Wiley, 2003).
- [28] K. J. Weatherill, Ph.D. thesis, Durham University (2007).
- [29] H. Merimeche, J. Phys. B **39**, 3723 (2006).
- [30] B. Lev, Y. Lassailly, C. Lee, A. Scherer, and H. Mabuchi, Appl. Phys. Lett. **83**, 395 (2003).
- [31] I. G. Hughes, P. A. Barton, T. M. Roach, and E. A. Hinds, J. Phys. B **30**, 2119 (1997).
- [32] E. A. Hinds and I. G. Hughes, J. Phys. D **32**, R119 (1999).
- [33] C. S. Adams, Private communication.
- [34] J. E. Lennard-Jones, Trans. Faraday Soc. **28**, 333 (1932).
- [35] F. London, Trans. Faraday Soc. **33**, 8b (1937).
- [36] H. B. G. Casimir and D. Polder, Phys. Rev. **73**, 360 (1948).
- [37] A. Landragin, J. Y. Courtois, G. Labeyrie, N. Vansteenkiste, C. I. Westbrook, and A. Aspect, Phys. Rev. Lett. **77**, 1464 (1996).
- [38] R. Marani, L. Cognet, V. Savalli, N. Westbrook, C. Westbrook, and A. Aspect, Phys. Rev. A **61**, 053402 (2000).
- [39] E. M. Lifshitz, JETP **2**, 73 (1956).
- [40] I. E. Dzyaloshinskii, E. M. Lifshitz, and L. P. Pitaevskii, Adv. Phys. **10**, 165 (1961).
- [41] A. K. Mohapatra, Ph.D. thesis, Tata Institute of Fundamental Research (2005).
- [42] R. A. Faulkner, Phys. Rev. **184**, 713 (1969).
- [43] T. Hayward, Private communication.
- [44] A. K. Mohapatra, S. Chaudhuri, S. Roy, and C. S. Unnikrishnan, Eur. Phys. J. D **42**, 287 (2007).
- [45] A. K. Mohapatra and C. S. Unnikrishnan, Pramana **66**, 1027 (2006).
- [46] T. M. Roach, H. Abele, M. G. Boshier, H. L. Grossman, K. P. Zetie, and E. A. Hinds, Phys. Rev. Lett. **75**, 629 (1995).
- [47] D. A. Allwood, Private communication.
- [48] D. M. Brink and C. V. Sukumar, Phys. Rev. A **74**, 035401 (2006).
- [49] F. S. Levin, *An introduction to quantum theory* (Cambridge, 2002).
- [50] J. R. Ensher, Ph.D. thesis, University of Colorado (1998).
- [51] W. Petrich, M. H. Anderson, J. R. Ensher, and E. A. Cornell, Phys. Rev. Lett. **74**, 3352 (1995).
- [52] E. Hodby, G. Hechenblaikner, O. M. Maragoò, J. Arlt, S. Hopkins, and C. J. Foot, J. Phys. B **33**, 4087 (2000).
- [53] S. Gov and S. Shtrikman, Am. J. Phys. **68**, 334 (2000).
- [54] M. Buttiker, Phys. Rev. B **27**, 6178 (1983).
- [55] C. Zener, Proc. R. Soc. Lond. **137**, 696 (1932).
- [56] P. W. Courteille, B. Deh, J. Fortágh, A. Günther, S. Kraft, C. Marzok, S. Slama, and C. Zimmerman, J. Phys. B **39**, 1055 (2006).
- [57] O. Zobay and B. M. Garraway, Phys. Rev. Lett. **86**, 1195 (2001).
- [58] I. Lesanovsky, S. Hofferberth, J. Schmiedmayer, and P. Schmelcher, Phys. Rev. A **74**, 033619 (2006).
- [59] S. Hofferberth, I. Lesanovsky, B. Fischer, J. Verdu, and J. Schmiedmayer, Nature Physics **2**, 710 (2006).
- [60] T. Schumm, S. Hofferberth, L. M. Andersson, S. Wildermuth, S. Groth, I. Bar-Joseph, J. Schmiedmayer, and P. Krüger, Nature Physics **1**, 57 (2005).
- [61] O. Morizot, C. L. Garrido, P. Pottie, V. Lorent, and H. Perrin, J. Phys. B **40**, 4013 (2007).
- [62] I. Lesanovsky, T. Schumm, S. Hofferberth, L. M. Andersson, P. Krüger, and J. Schmiedmayer, Phys. Rev. A **73**, 033619 (2006).
- [63] T. Schreffl, M. E. Schabes, D. Suess, and M. Stehno, IEEE Trans. Magn. **40**, 2341 (2004).
- [64] P. Castrucci, R. Gunnella, P. Candeloro, E. Di Fabrizio, M. Conti, G. Carlotti, G. Gubbiotti, F. Montoncello, R. Zivieri, M. Scarselli, et al., Surface Science **566-568**, 291 (2004).
- [65] I. G. Hughes, *New Trends in Quantum Coherence and Nonlinear Optics* (Nova Publishers, 2009), vol. 263 of *Horizons in World Physics*, chap. 5, polarization spectroscopy of alkali-metal atoms.
- [66] H. D. Do, G. Moon, and H. Noh, Phys. Rev. A **77**, 032513 (2008).
- [67] M. L. Harris, C. S. Adams, S. L. Cornish, I. McLeod, E. Tarleton, and I. G. Hughes, Phys. Rev. A **73**, 062509 (2006).
- [68] D. E. Pritchard, Phys. Rev. Lett. **51**, 1336 (1983).
- [69] Y. V. Gott, M. S. Ioffe, and V. G. Tel'kovskii, Nuclear Fusion **Suppl. 2**, 1045 (1962).
- [70] W. Ketterle, D. S. Durfee, and D. M. Stamper-Kurn, ArXiv e-prints (1999), cond-mat/9904034 v2.
- [71] I. S. Grant and W. R. Phillips, *Electro-magnetism* (Wiley, 2003), 2nd ed.
- [72] M. Key, I. G. Hughes, W. Rooijakkers, B. E. Sauer, and E. A. Hinds, Phys. Rev. Lett. **84**, 1371 (2000).